Electron Bernstein Wave Heating of Overdense H-mode Plasmas in the TCV Tokamak via O-X-B Double Mode Conversion

A. Pochelon[1], A. Mueck[1], Y. Camenen[1], S. Coda[1], L. Curchod[1], B.P. Duval[1], T.P. Goodman[1], I. Klimanov[1], H. Laqua[2], Y. Martin[1], J.-M. Moret[1], L. Porte[1], A. Sushkov[3], V.S. Udintsev[1], F. Volpe[2] and the TCV Team

[1]Ecole Polytechnique Fédérale de Lausanne (EPFL), Centre de Recherches en Physique des Plasmas, Association EURATOM-Confédération Suisse, CH-1015 Lausanne, Switzerland
[2]Max Planck Institut für Plasmaphysik, IPP-Greifswald, D-17491 Greifswald, Germany
[3]RRC "Kurchatov Institute", Nuclear Fusion Institute, 123182 Moscow, Russia

e-mail contact of main author: Antoine.Pochelon@epfl.ch

Abstract. The first demonstration of Electron Bernstein Wave (EBWH) Heating by double mode conversion from ordinary (O-) to Bernstein (B) via extraordinary (X-)mode in an over-dense tokamak plasma, using low field side (LFS) launch, has been achieved in the TCV tokamak. This technique offers the possibility of overcoming the upper density limit of conventional EC microwave heating. The sensitive dependence of the O-X mode conversion on the microwave launching direction has been verified experimentally, and localised power deposition consistent with theoretical predictions has been observed at densities well above the conventional cut-off. Central heating has been achieved, at powers up to two megawatts. This demonstrates the potential of EBW in tokamak H-modes, the intended mode of operation of a reactor such as ITER.

1. Introduction

A high plasma density will be beneficial to the fusion power yield in a thermonuclear reactor both directly, by increasing the reaction rate, and indirectly, by increasing the plasma confinement, according to well-established experimental scaling laws. The heating of high-density plasmas with Electron Cyclotron Resonance Heating (ECRH) is, however, limited by the reflection of the microwaves at so-called wave cut-offs [1]. In contrast, the electrostatic Bernstein mode encounters no density cut-off in the plasma, but cannot propagate in vacuum and must thus be excited by mode conversion. The double mode conversion scheme from O-mode to X-mode and finally to Bernstein mode (O-X-B) is examined in this paper [2, 3].
The accessibility of EC waves depends primarily on the magnetic field, which determines the required frequency of power sources. We compare the EC waves accessibility in tokamak-like machines, from the low field spherical tokamaks (B=0.5T), through medium field TCV (B=1.5T, R=0.88m, a=0.25m), to the high field ITER machine (B=5.3T) [4]. The accessibility limitation due to EC cut-offs is compared to the empirical Greenwald density limit $\langle n_{eG}\rangle = 0.27 \cdot I_p/a^2$ [5], where I_p is the plasma current and a the plasma radius. For the comparison, I_p is taken using shaping parameters such the safety factor, elongation and triangularity (q_{95}=3, κ=1.85, δ=0.5) from the standard ITER operation model.
In spherical tokamaks, the low ECW harmonics may only access densities up to a few percent of n_{eG}, so another heating scheme such as EBW has great potential. In the medium field machine TCV, 10% of n_{eG} is accessible with the 2nd harmonic X-mode (X2), which has been successfully extended to 25% using 3rd harmonic X-mode (X3) [6]. The density range above O2 and X3 density limits can be accessed with EBWs, for instance using the 2nd harmonic as described in this paper. In ITER, the magnetic field is sufficient to permit heating of the intended operational density range using the fundamental O-mode (O1) at 170GHz. Current drive applications using EBWs, with potentially more efficiency than ECCD [7,8] and benefiting of the same localised deposition properties, could still make EBW attractive.

In the used conversion scheme, a quasi-circularly polarised O-mode wave is injected at a particular angle, converts at the plasma cut-off into the X-mode and propagates back to the upper hybrid resonance. Close to this resonance, the X-mode converts into the electrostatic Bernstein mode, which then propagates towards the plasma centre where it is absorbed at harmonics of the EC resonance. For a hot plasma, this second conversion has an efficiency of ~100%. The O- to X-mode conversion efficiency, however, depends on the O-mode wave injection angle and may be characterised by the power transmission function T from O- to X-mode, derived by Mjølhus [9]:

$$T(N_\perp, N_\parallel) = \exp(-\pi k_0 L_n (Y/2)^{1/2}[2(1+Y)(N_{\parallel,opt}-N_\parallel)^2+N_\perp^2]) \qquad \text{(Eqn. 1)}$$

with a radial density-gradient scale length $L_n=n_e/(\partial n_e/\partial x)$, the refraction indices perpendicular $N_\perp$ and parallel $N_\parallel$ to the local magnetic field and $Y=\omega_{ce}/\omega$ with the electron cyclotron frequency ω_{ce} and the wave frequency ω. Only at the optimum $N_{\parallel,opt}^2=Y/(Y+1)$ and $N_\perp^2=0$, corresponding to an optimum injection angle, can the O-mode wave be completely converted to X-mode. For non-optimal injection, the O-X conversion efficiency decreases with increasing L_n. The wave energy that is not mode converted reflects back towards the plasma edge and either escapes the device or contributes via multi-pass absorption.
This heating scheme is not new. Electron Bernstein Wave Heating (EBWH), with O-X-B double mode conversion scheme, was successfully demonstrated in the W7-AS stellarator [10], with injection into a High Density High confinement (HDH) mode. Electron Bernstein Emission (EBE) measurements in spherical, low aspect-ratio tokamaks and in reversed field pinches are reported in [11-13]. High field side (HFS) launch Bernstein wave heating was demonstrated in a tokamak using the X-B scheme [9], but this scheme is limited by the left-hand X-mode cut-off. Over-dense plasma heating was demonstrated in a spherical tokamak using the X-B scheme from the LFS with the X-mode tunnelling through the evanescent layer with L_n artificially reduced by a local limiter [15]. These experiments in TCV, however, demonstrate EBWH, for the first time, in a conventional-aspect-ratio tokamak, with O-X-B double mode conversion, with the requisite low L_n values (high density gradient) obtained in the High-confinement mode (H-mode) [16].

2. Experimental set-up

2.1 TCV ECH system and diagnostics

The TCV tokamak is equipped with 4.5MW ECH nominal power for pulse lengths of 2s: 3MW at the 2nd harmonic (X2) and 1.5MW at the 3rd harmonic (X3) not described here. The X2 system features six 475kW gyrotrons at a frequency of 82.7GHz equipped with six low field side (LFS) launchers installed on upper lateral (4) and equatorial ports (2). All 6 launchers are independently steerable during the discharge, each with two degrees of freedom, the two "launcher angles" τ and π parametrising the beam directions.
At the axial TCV magnetic field of B = 1.5T, the cut-off densities for X2, O2 and X3 waves are 4.2, 8.7 and $11.1\cdot10^{19}m^{-3}$ respectively. This paper explores the potential of EBW at densities above the O2 cut-off with high power. Three diagnostics are used to measure the power absorption. The reflected EC power, scattered inside the torus, is measured by several semiconductor diodes, installed in several sectors of TCV. Using power modulation techniques [17], the total absorbed power is measured by a diamagnetic loop (DML) [18], and the local deposition [19,20] is measured with a high spatial resolution, 64-channel, soft X-ray wire chamber (DMPX) viewing the plasma vertically, with a Krypton gas fill and sensitive in the 2-25keV range (10% efficiency limits) [21].

2.2 Optimisation of H-mode discharges for EBW coupling

To achieve a large angular window of the O-X power transmission function, the density scale length at the plasma cut-off must be reduced, implying a steep density gradient, see Eqn (1). This is available in the edge pedestal of TCV H-modes (small L_n) with typically low q_{95}=2.2-2.4, high triangularity δ=0.5-0.6, medium elongation κ=1.8 (with I_p=415kA, 1.2<B<1.4T, $n_{eo} \geq 1 \cdot 10^{20}$ m^{-3} equivalent with n_{eo}/n_{eoG}~0.4-0.6). Low q, high δ, and high n_e, together with high power, are known to favour high edge density gradients and thus lower L_n [22]. Low-q H-modes, however, often exhibit strong MHD activity: large central sawteeth and edge localised modes (ELMs). This strong core activity can hamper the diagnostics measuring local power deposition in the plasma centre. To date, the most successful TCV discharges are non-stationary, with the density generally continually increasing.

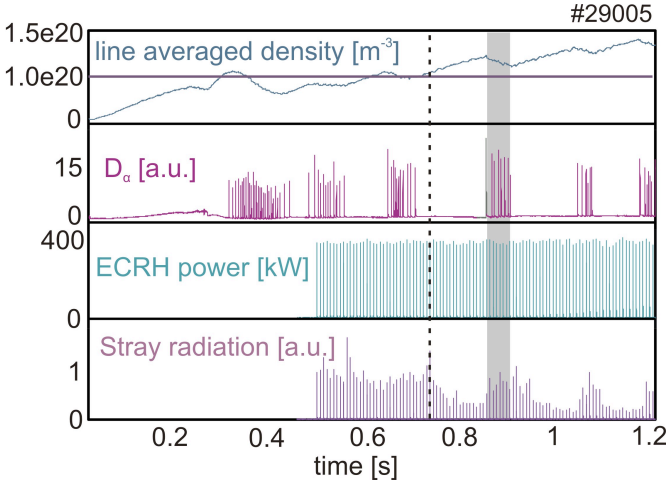

FIG. 1: Typical high-density ELMy H-mode target plasma with alternating ELM-free phases. Modulated EC waves are injected. When the plasma becomes over-dense, the stray level becomes low in the ELM-free phases, indicating increased O-X power conversion, and higher in the ELMy phases. The highlighted region is detailed in FIG. 2.

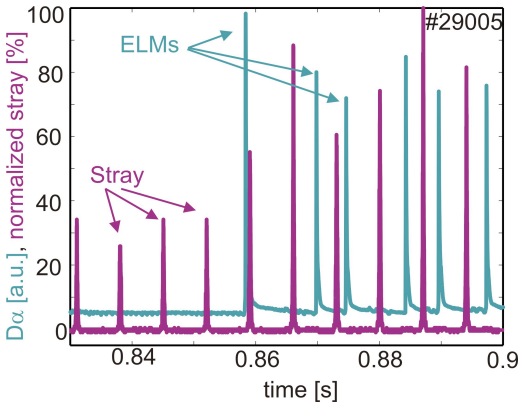

FIG. 2: Normalised stray radiation power (violet) and D_α-light emission (green). ELMs can strongly influence the stray radiation. The stray power, measured during the short EC pulses, rises from 30% to 80% during an ELMy phase.

For these discharges, the O2 density cut-off typically occurs at $\rho_\psi \sim 0.9$, in the steep edge density gradient region. A typical high-density target plasma is shown in *FIG. 1*, where the H-mode exhibits alternating ELMy/ELM-free phases. The coupled line-averaged density and density gradient rise during the ELM-free phases and drop during the ELMy phase. To avoid strong perturbation of the H-mode, 500 kW modulated EC power was injected with a low duty cycle of 6%. The stray radiation level, plotted in *FIG. 1*, decreases with increasing density which is indicative of an increase of the EC power absorption. The increase in the density gradient broadens the angular window for the O-X mode conversion, (see Eqn 1). The stray level is observed to increase rapidly with the first ELM, suggesting diminished EC conversion, presumably caused by ELM induced decrease in both the density and density gradient (*FIG. 2*).

3. Experimental Determination of Optimum Injection Angle

A single ray simulation with the non-relativistic ART ray-tracing code [23,24], including O-X-B double mode conversion for wave propagation and absorption, was performed for the target plasma conditions, to determine the optimal poloidal and toroidal injection angles.
Around these theoretical optimal angles, experimental scans along the two "launcher angles" τ and π were performed on a shot to shot basis to measure the plasma reaction. For an equatorial launch and for one of the launcher angles (here τ), clear minima in the stray radiation level are found, see *FIG. 3a*, indicating the power absorption maxima, which are interpreted as a measure of the optimal angles. We project these angles into the conventional toroidal and poloidal angles (φ_{tor} and φ_{pol} = 0 for an injection in the poloidal plane and in horizontal direction, respectively). The optimum toroidal angle is then approximately 26°, see *FIG. 3b*. Comparable angle dependence in the stray radiation is found for both upper lateral and equatorial launchers in all stray radiation diode signals around the torus.
The experimentally determined optimum angles are again compared with the ART ray tracing code. In *FIG. 4*, the simulated O-X conversion efficiency is shown in a contour plot. The innermost contour indicates 90% conversion, the outermost contour 10%. The experimental angles of the τ and π-scans for the equatorial port launch are indicated as violet dots and the extrapolated optimum angle as a green dot. This experimental optimum angle is in good agreement with the simulated angle within 2°. This small discrepancy can be explained partly by the resolution of the scans (the angles can be set with 0.2° precision) and more significantly by the imprecision of the magnetic equilibrium reconstruction of ~ ±1cm. When such an equilibrium shift is applied to the ART simulation, the optimum angles shift by ~ ±1°.

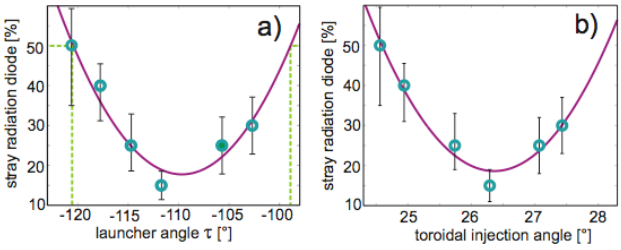

FIG. 3: a) Normalised stray radiation power vs. "launcher angle" τ and b) same scan projected on the toroidal angle. The solid curves represent polynomial regression fits to the data points. The dashed lines in FIG. 3a indicate the width of the 50% of maximum stray level. This width is about twice the ART single ray calculation width.

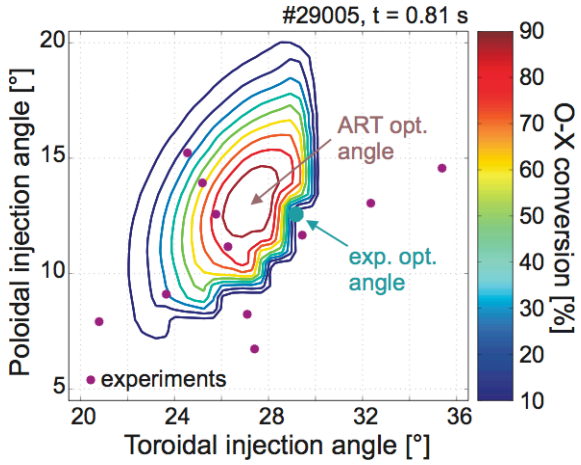

FIG. 4: Contour plot of calculated O-X power conversion efficiency vs. toroidal and poloidal angles (φ_{tor} and φ_{pol}). The innermost contour indicates 90% O-X conversion, the outermost 10%. The superimposed points give the angles of the experimental scans (see FIG. 3a, vs. τ). The green point corresponds to the extrapolated optimum experimental angles and is within 2° of the calculated optimum angles.

The experimental 50%-absorption width shown in *FIG. 3a* is somewhat larger than the simulation width. The discrepancy between the measured and calculated angular window size is not surprising in view of the finite width of the EC beam and the spread in its wave-number spectrum, which is expected to broaden the width of the conversion efficiency function and reduce its absolute value. This is also consistent with a measurable minimum stray level, implying that less than 100% of the beam power is absorbed.

In summary, the correspondence of the angular dependence and the agreement of the optimal angles between experiment and simulation, strongly indicate that O-X-B mode conversion is occurring [18-20].

4. Global and local Bernstein wave heating

Heating experiments were performed with the experimentally determined optimal angles. The duty cycle was increased to 46% with ~ 500 kW EC power injected for a modulation frequency of 182 Hz. This modulation frequency was chosen between the first (~110Hz) and second harmonics of the sawtooth instability.
A basic cross-check of the O-X transmission can be performed by comparing the stray radiation levels when power is injected in the vicinity of the optimum angles for O- and X-mode. For a similar ELM-free phase with EC power of ~ 450 kW, the stray level for O-mode injection was only 40% of that observed for X-mode injection, showing that considerably higher conversion efficiency is obtained with O-mode.
The overall absorbed power was measured with a diamagnetic loop [17], which measures the toroidal magnetic flux variation, which is related to the plasma stored energy. Absorption of typically 60% was obtained for O-mode injection whereas for X-mode, the absorption was below 10%. O-mode may thus be converted and penetrate into the plasma while the X-mode is reflected, as expected for over-dense plasmas. A total power absorption measurement cannot be used conclusively to prove the nature of the absorption mechanism, which could also involve edge absorption of waves generated by nonlinear wave-wave coupling and/or absorption of waves multiply reflected at the vacuum vessel. A determination of the power deposition location is essential to prove EBW heating.

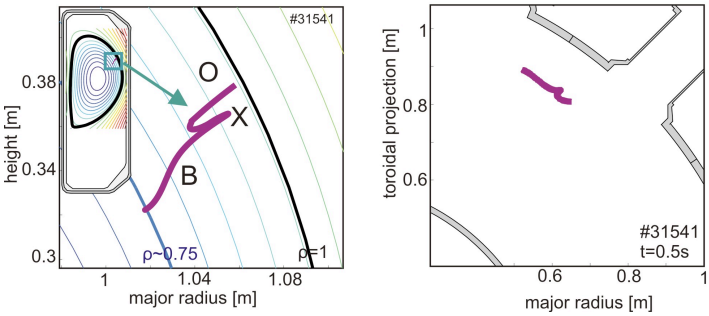

FIG. 5: ART ray tracing calculation of the wave path in a) poloidal and b) toroidal projections, including O-X-B double mode conversion.

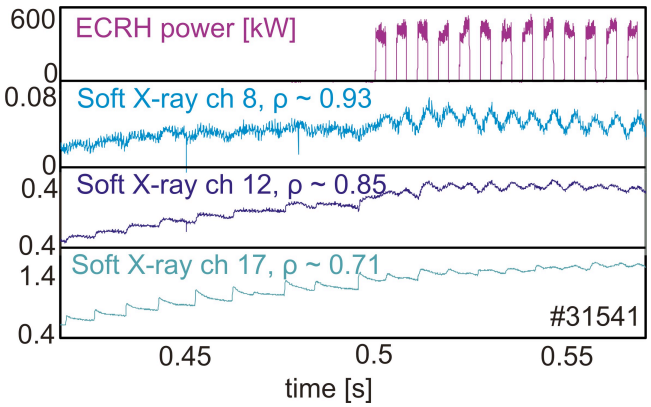

FIG. 6: The injection of modulated EC waves is directly visible on several radial soft X-ray time traces. To determine the deposition location, an FFT of each channel-trace is performed.

The plasma centre of the high-density target plasma is strongly affected by the sawtooth instability, which repeatedly expels heat from the hot plasma core towards the colder edge region. In the core of the plasma, close to this strong instability, proving power deposition from EBWH is extremely difficult so conditions for a deposition location off-axis, but still

well inside the plasma cut-off, were selected. In *FIG. 5*, an ART simulation of such a wave path is shown in poloidal and toroidal projection. The O-mode wave propagates to the plasma cut-off, is mode converted into X-mode and then returns to the upper hybrid resonance where it is converted into Bernstein wave. The B wave is then absorbed at $\rho_\psi \sim 0.78$, well inside the plasma cut-off layer at $\rho_\psi \sim 0.9$ (see *FIG. 7b*).

The deposition location is determined experimentally using the soft X-ray emission measured by a multi-wire proportional detector with its multiple lines of sights in the vertical direction, covering the entire plasma cross-section. For these conditions the soft X-ray emissivity increases monotonically with the electron temperature and density. In *FIG. 6*, the heating effect caused by the modulated EC power is visible in the line-integrated time traces of several channels, on both the HFS and LFS. The deposition location is located using an FFT analysis of the 64 soft X-ray chords signals. The FFT amplitude of the peak at the EC modulation frequency is plotted against the soft X-ray channel number in *FIG. 7a*. Two clear amplitude peaks are visible. These broad spatial peaks correspond to emission at $\rho_\psi \sim 0.65$, on both the HFS and LFS. The maximum on the HFS is more pronounced due to the geometrical effects of line integration and the field line compression with positive plasma triangularity.

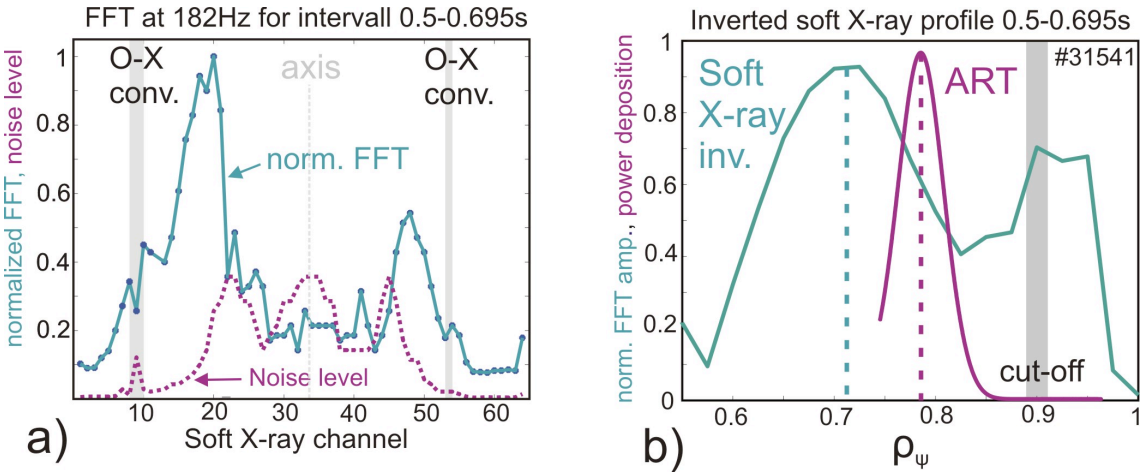

FIG. 7: a) Normalised FFT amplitude of the line-integrated soft X-ray time traces at the modulation frequency (182 Hz) of the injected EC waves, vs. the chord number (green). The "noise" level (essentially due to sawteeth) is shown for reference (violet). b) Normalised FFT amplitude of the local soft X-ray emissivity at the modulation frequency, derived by integral inversion of the line-integrated soft X-ray chord signals (green) demonstrating over-dense deposition at $\rho_\psi \sim 0.71$. The normalised density of the deposited beam power, calculated with single ray ART calculation, is also indicated confirming EBW absorption well inside the cut-off at $\rho_\psi \sim 0.78$.

Since the soft X-ray signals are line-integrals of the local emissivity, the profile is inverted to derive the local emissivity distribution. This is accomplished assuming poloidal homogeneity and imposing the Fisher regularisation algorithm. *FIG. 7b* plots the FFT amplitude of the inverted data at the EC modulation frequency against the poloidal flux radial coordinate ρ_ψ. The peak of the FFT amplitude, after inversion, is located at $\rho_\psi \sim 0.71$, inside the plasma cut-off. This experimental peak deposition location is close to that calculated at $\rho_\psi \sim 0.78$, i.e. within 10% of radial coordinate. The slight difference may again be attributed to uncertainties in the equilibrium reconstruction and the density gradient measurement. In addition, the edge soft X-ray signals indicate some residual power deposited outside cut-off, presumably resulting from 2nd harmonic X-mode absorption of non-converted wave power possibly after multiple wall reflections.

Again, the good agreement between the theoretical and experimental deposition locations, together with deposition at an over-dense location, constitutes strong proof that the O-X-B conversion mechanism is at play.

5. Central Electron Temperature increase by long pulse EBWH

To be able to observe the EBH effects, such as an increase of the central temperature, the pulse duration was extended to 100ms, i.e. for several energy confinement times (τ_E~50ms), and the power increased to 2MW with a modulation depth of 1MW, as shown in *FIG. 8*. Here, 4 independent launchers were employed. The injection angles were chosen such that both upper lateral and equatorial launchers heat at the same location at $\rho_\psi \sim 0.4$ (calculated by ART); particular care was taken to ensure that the two modulated beam locations coincided. A more central deposition was achieved by lowering the machine magnetic field to 2T to displace the 2nd harmonic cold resonance further to the HFS.
TCV is equipped with 3 centrally aimed soft X-ray diodes equipped with varying beryllium thicknesses which are used to measure the electron temperature by the absorber method. All diode arrays showed an increase of the electron temperature $\Delta T_e \sim 80$eV during the EC pulse (*FIG 8*). With the total injected power of 2MW, large ELMs develop at a slow repetition rate (16ms), that result in a near constant plasma density (unlike the case with fast ELMs at lower power). The slowly increasing density during the pulse allows the temperature increase to be directly attributed to EBWH. The temperature increase is also seen by Thomson scattering measurements. *FIG. 9* shows two Thomson temperature profiles at 1.0s, before ECH modulation, and at 1.1s during ECH modulation. The evident increase in the central temperature is in agreement with the soft X-ray absorber measurement.

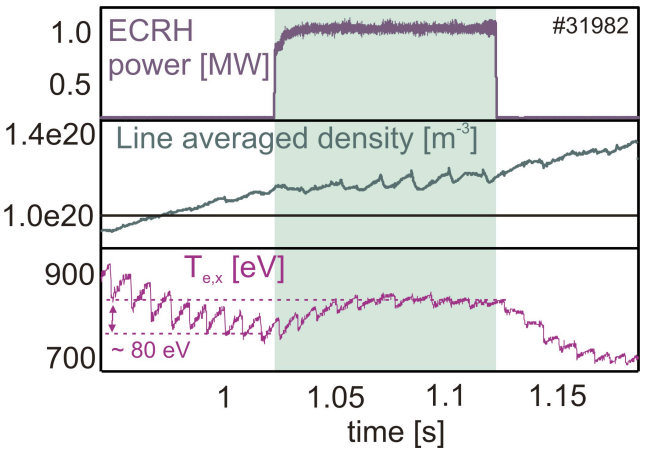

FIG. 8: Long EC power modulation pulses of 100 ms, on top of 1MW CW (not shown), demonstrating a temperature increase due to EBWH, measured by the soft X-ray absorber method. The essentially constant density, supports attributing the temperature increase to EBWH.

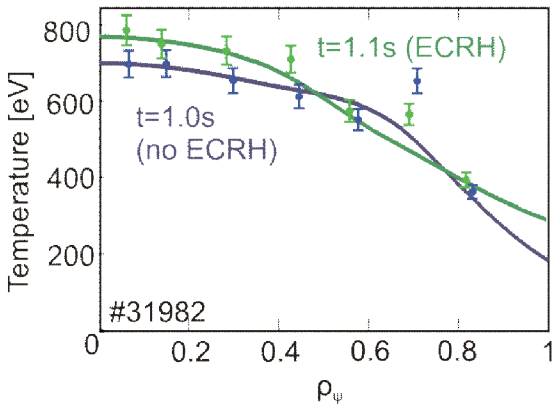

FIG. 9: Electron temperature profiles before the modulation EC power pulse (1.0s) and during the modulation EC pulse (1.1s), from Thomson scattering.

7. Conclusions and Outlook

EBW heating by O-X-B double mode conversion in an over-dense conventional aspect-ratio tokamak has been demonstrated in TCV. The optimal injection angles for O-X-B conversion were determined experimentally by 2D angle scans by minimising the microwave stray radiation levels in discharges with low duty cycle modulated EC wave injection. Simulations

with the ART ray tracing and double mode conversion code were performed demonstrating excellent agreement between the simulated and measured angles.
Higher duty cycle modulated EC waves were injected to measure global and local EBWH power deposition. A global absorbed power fraction of ~60% was measured from the diamagnetic probe with densities well above the cut-off. The spatial distribution of the local power absorption was determined experimentally by FFT analysis of soft X-ray emissivity signals. The deposition radius, well inside the plasma cut-off, matches the value predicted by ART to within the experimental uncertainties. These modulated power deposition measurements were designed with a relatively far off-axis deposition, at ρ_ψ=0.7, to avoid the strong sawtooth perturbations that hamper a central detection of the local power deposition. Long pulse power deposition, for periods of many confinement times, was achieved with a lowered magnetic field to obtain a more central power deposition, ρ_ψ=0.4. Corroborating central temperature increases were from Thomson scattering and the soft X-ray absorber measurements.
In summary, the experiments presented here demonstrate for the first time that EBWH can be used in a conventional aspect ratio tokamak, in H-mode, utilising the naturally occurring steep density gradients.

Acknowledgments: This work was supported in part by the Swiss National Science Foundation. A. Mueck was supported by a EURATOM Fusion fellowship.

References

[1] STIX, T.H., Waves in Plasmas, Springer Verlag New York, Inc., 1992.
[2] BERNSTEIN, I., Phys. Rev. Lett. **109** (1958) 10.
[3] PREINHAELTER, J., KOPECKY, V., J. Plasma Physics **10**, part 1 (1973) 1.
[4] POCHELON, A., et al., Proc. 6th Int. Workshop on "Strong Microwaves in Plasmas", Nizhny Novgorod 2005, ed. A.G. Litvak, Vol. **2**, 421.
[5] GREENWALD, M., et al., Nucl. Fus. **28** (1988) 2199.
[6] PORTE, L., CODA, S., ALBERTI et al., this Conf., EX/P6-20.
[7] RAM, A., DECKER, J., PEYSSON, Y., J. Plasma Phys. **71** (2005) 675.
[8] SHEVCHENKO, V., BARANOV, Y., O'BRIEN, et al., Phys. Rev. Lett. **89** (2002) 265005.
[9] MJØLHUS, E., J. Plasma Phys**. 31** (1984) 7.
[10] LAQUA, H.P., et al., Phys. Rev. Lett. **78** (1997) 3467.
[11] CHATTOPADHYAY, P.K., et al., Phys. Plasmas **9** (2002) 752.
[12] TAYLOR, G., et al., Phys. Plasmas **12** (2005) 052511.
[13] SHEVCHENKO, V., et al., 15th Conf. RF Power in Plasmas, ed. C. Forrest, AIP Conf Proc. **694**, 359.
[14] McDERMOTT, F., BEKEFI, G., HACKETT, K., LEVINE, J., PORKOLAB, M., Phys. Fluids **25** (1982) 1488.
[15] SHIRAIWA, S., HANADA, K., HASEGAWA, M., et al., Phys. Rev. Lett. **96** (2006) 185003.
[16] WAGNER, F., et al., Phys. Rev. Lett. **49** (1982) 1408.
[17] MANINI, A., MORET, J.-M., et al., Plasma Phys. Control. Fusion **44** (2002) 139.
[18] MUECK, A., et al., Proc. 32nd Eur. Conf. on Plasma Phys. and Contr. Fusion, Tarragona, 2005, P4.110.
[19] MUECK, A., et al., EC–14, 14th Joint Workshop on ECE and ECRH, Santorini, Greece, 2006.
[20] MUECK, A., et al., Proc. 33rd Eur. Conf. on Plasma Phys. and Contr. Fusion (Rome, 2006).
[21] SUSHKOV, A., CAMENEN, Y. et al., 29th EPS (ibid.) ECA Vol. 26B (2002) P-4.118, to be published.
[22] HUGHES J.W., MOSSESSIAN D.A., et al., Physics of Plasmas **9** (2002) 3019.
[23] VOLPE, F., PhD thesis, IPP Garching and Greifswald, IPP Report 13/1, March 2003.
[24] VOLPE, F., LAQUA, H.P., and the W7-AS Team, Rev. Sci. Instrum. **74** (2003) 1409.